Smart Mater. Struct. **19** (2010) 055006 (13pp) doi:10.1088/0964-1726/19/5/055006

Purified and porous poly(vinylidene fluoride-trifluoroethylene) thin films for pyroelectric infrared sensing and energy harvesting

A Navid, C S Lynch and L Pilon

Mechanical and Aerospace Engineering Department, Henry Samueli School of Engineering and Applied Science, University of California, Los Angeles, Los Angeles, CA 90095, USA

E-mail: pilon@seas.ucla.edu

Received 20 October 2009, in final form 4 February 2010
Published 23 March 2010
Online at stacks.iop.org/SMS/19/055006

Abstract

This paper aims at improving the performance of the poly(vinylidene fluoride-trifluoroethylene) [P(VDF-TrFE)] copolymer for pyroelectric infrared detection and direct thermal to electrical energy conversion. Three different types of samples were prepared and examined: commercial, purified and porous films. Here, full characterization of the thermophysical and electrical properties relevant to pyroelectric infrared detection and energy conversion of both purified and porous P(VDF-TrFE) thin films is presented. Properties measured include (1) density, (2) ferroelectric to paraelectric phase transition temperature, (3) enthalpy of change of phase, (4) electrical resistivity and (5) ferroelectric hysteresis, as well as (6) specific heat, (7) dielectric constant, (8) loss tangent and (9) pyroelectric coefficient as a function of temperature. The figures of merit for infrared detection F_V, F_I and F_D were improved by 47.0, 59.6 and 51.6%, respectively, for the purified films while the porous films with a porosity of 33% showed an improvement of 52.8, 66.3 and 62.6%, respectively, when compared to those of dense commercial P(VDF-TrFE) films. In addition, figures of merit for energy harvesting, F_E and k^2, indicate that the purified and porous films are attractive for thermal to electrical energy conversion as well.

1. Introduction

Poly(vinylidene fluoride) PVDF and its copolymer with trifluoroethylene P(VDF-TrFE) have received special attention over other pyroelectric polymers as they can be implemented from industrial to biomedical applications [1]. The ferroelectric behavior, along with lower cost, make both of these polymers viable alternatives to ceramics like PZT. Typical applications for materials such as PVDF and P(VDF-TrFE) include infrared detection [1–4], infrared imaging [1, 5–7] and, to a lesser extent, heat to electricity conversion [1, 8–22].

The performance of pyroelectric materials in these applications depends strongly on the material's thermophysical and electrical properties. For P(VDF-TrFE), these properties have been studied for various VDF and TrFE compositions. For example, Furukawa *et al* [23] measured the specific heat and dielectric constant of 55 mol% VDF and 45 mol% TrFE or 55/45 P(VDF-TrFE) films between 20 and 100 °C and the ferroelectric hysteresis at 20 °C. Yamazaki *et al* [24] reported the pyroelectric coefficient of 51/49 P(VDF-TrFE) films at room temperature. Furukawa *et al* [25] examined the ferroelectric hysteresis and dielectric constant of 52/48 P(VDF-TrFE) films between 20 and 100 °C. Davis *et al* [26] measured the ferroelectric hysteresis of 65/35 and 73/27 P(VDF-TrFE) films between 23 and 70 °C, along with the ferroelectric to paraelectric phase transition temperature and enthalpy change. More recently, Wong *et al* [27] studied the density, specific heat and thermal conductivity of 70/30 and 56/44 P(VDF-TrFE) films between −73 and 117 °C.

Pyroelectric infrared detectors demand linearity and their performance has been shown to increase by maximizing the pyroelectric coefficient and minimizing the density, specific heat and dielectric loss [1, 28]. For energy harvesting,

several efforts have been made to improve the efficiency and power density as well as to reduce the cost of pyroelectric converters by replacing PZST with polymeric pyroelectric materials [13, 15, 29, 30]. Olsen *et al* [13] reported that vacuum baking P(VDF-TrFE) helps remove any residual solvent and improves both dielectric strength and electrical resistivity. Kouchachvili *et al* [15, 31] used a proprietary purification process for P(VDF-TrFE) which removed approximately '0.4% of unidentifiable impurities' and increased the electrical resistivity of the material by 35%, resulting in 'nearly a threefold increase in energy density from 95 to 279 $J\,l^{-1}$'. The authors reported phase transition temperature, enthalpy of change of phase and electrical resistivity for purified P(VDF-TrFE). Vanderpool *et al* [32] numerically showed the efficiency of a prototypical pyroelectric converter [8] can be increased by reducing the product of the density and specific heat ρc_p of both the pyroelectric material and the working fluid while the power density can be increased by reducing the product ρc_p of the pyroelectric material and increasing that of the working fluid.

This work reports for the first time, to the best of our knowledge, full thermophysical and electrical characterization of 60/40 wt% P(VDF-TrFE) films. Properties measured include (1) density, (2) ferroelectric to paraelectric phase transition temperature, (3) enthalpy of change of phase, (4) electrical resistivity and (5) ferroelectric hysteresis, as well as (6) specific heat, (7) dielectric constant, (8) loss tangent and (9) pyroelectric coefficient as a function of temperature. Furthermore, this study proposes to introduce pores into the 60/40 P(VDF-TrFE) matrix in order to reduce the density and specific heat of the copolymer and improve its performance for infrared detection and energy conversion. In addition, since the purification process proposed by Kouchachvili *et al* [15, 31] has shown promise for energy conversion, its effect on infrared detection is explored here as well.

2. Experimental details

2.1. Film preparation

The following subsections detail the processes for preparing (i) dense films from commercial P(VDF-TrFE) pellets, (ii) purified films and (iii) porous films used in this study. The process for all films uses the commercial copolymer of 60/40 P(VDF-TrFE), purchased in pellet form from Chronos Research Laboratories, Inc., San Diego, CA, USA.

2.1.1. Commercial dense P(VDF-TrFE) films. A custom press was utilized to form the pellets into thin films. It consisted of a hydraulic press (model 3912 by Carver Inc., USA), a custom-made hot plate and two steel dies. The hot plate consisted of an aluminum plate hosting a 100 W cartridge heater. Two sheets of Kapton® HN film were used to prevent the copolymer from sticking to the steel dies. In addition, two slabs of concrete placed below the hot plate and above the top die acted as thermal insulation to prevent the dies from cooling too quickly.

The forming process began by heating the two steel dies covered with Kapton® HN films on the hot plate until the temperature reached 185 °C. This is above the copolymer melting temperature of 155 °C. Then, a single P(VDF-TrFE) pellet, about 4 mm in length and 2 mm in diameter, was placed between the dies and transferred to the hydraulic press where a load of ∼8900 N (∼2000 lb) was applied. The temperature was kept constant at 185 °C for 2 min and then the hot plate was turned off. After the temperature of the dies decreased below 70 °C, the load was removed. The resulting film was approximately 50 μm thick. Next, the film was baked in a vacuum oven (model 1415M by Sheldon Manufacturing, Inc., USA) at 130 °C and approximately 1 Torr (133 Pa) for 24 h to remove solvents and volatile impurities, and to improve both the dielectric strength and resistivity [13]. Then, a 10 nm thick titanium film was deposited onto both sides of the film as an adhesion layer for the subsequent deposition of 1 μm thick aluminum electrodes. The deposition of both metals was done by electron beam evaporation using an evaporator model Mark 40 by CHA Industries, USA. Afterwards, a wire was attached to the aluminum electrodes on each side of the film using copper tape. A type J thermocouple was also attached to the film in such a way that it was in thermal, but not in electrical, contact with the electrodes.

2.1.2. Purified P(VDF-TrFE) films. Solvent extraction was used to purify the copolymer P(VDF-TrFE) in order to reduce internal leakage at high temperature and voltage caused by the presence of impurities. The process was inspired from [15, 31]. It began by dissolving 0.5 g of commercial pellets of 60/40 P(VDF-TrFE) in 12 ml of methyl ethyl ketone (MEK, 99.6%, supplied by Mallinckrodt, USA) in a small glass beaker to create a homogeneous solution. The solution was continuously stirred at 70 °C for approximately 45 min. When all of the copolymer had dissolved, the temperature was increased to 140 °C and the solution was boiled for 20 min to increase its viscosity. Next, the viscous solution was poured into a separatory funnel containing 100 ml of anhydrous ethanol (EtOH, supplied by Acros Organics, Belgium). The mixture was then vigorously shaken and left to sit for 3 h to allow the copolymer particulate to precipitate and separate from the solvent. Then, the copolymer was drained from the bottom of the separatory funnel onto filter paper (Whatman paper filter No. 42) and approximately 3 h were allowed for the copolymer to precipitate as gel. The gel was thoroughly rinsed with EtOH. Then the gel was air dried in an oven at 50 °C and atmospheric pressure for 3 h and further air dried at room temperature in a fume hood for three days. The solid copolymer gel was then cut into small pieces. Finally, the same procedure described in section 2.1.1 was followed to form the pieces into thin films and to deposit electrodes, wires and attach a thermocouple.

2.1.3. Porous P(VDF-TrFE) films. Phase inversion is a widely used process for creating porous and nonporous polymer membranes or thin films [33]. It allows for the controlled conversion of a polymer from a liquid to a solid state. First, the polymer is dissolved with a suitable solvent to form a viscous liquid solution. The conversion from liquid to solid is then achieved through immersion precipitation [34–37]. In this process, the viscous solution

is cast as a thin film on a substrate, and then submerged in a nonsolvent (a chemical miscible with the solvent). The solvent diffuses out of the film while the nonsolvent diffuses into the cast film [33]. As time progresses, the exchange between the solvent and nonsolvent reaches a point when the solution becomes thermodynamically unstable, leading to demixing and subsequent precipitation of the polymer. The film morphology depends on the type of demixing process that occurs. For porous films, instantaneous liquid–liquid demixing is required [33]. In this process, the film is formed immediately after submersion in the nonsolvent bath.

Bottino *et al* [38] successfully synthesized porous thin films of PVDF using immersion precipitation. The authors were able to make PVDF films approximately 200 μm thick with porosities between 65 and 88%. The same technique was used here to synthesize porous thin films of P(VDF-TrFE).

The process began by preparing the substrate. The substrate consisted of a 2 inch silicon wafer wrapped in aluminum foil since it provided good adhesion with the copolymer film. The aluminum covered wafer was baked at 150 °C for at least 10 min to remove moisture and increase the subsequent adhesion of the copolymer film. Next, about 0.5 g of commercial 60/40 P(VDF-TrFE) pellets were cut into small pieces, to reduce dissolving time, and were dissolved in ∼3.5 ml of MEK in a small glass beaker to create a 15 wt% solution of P(VDF-TrFE). The mixture was heated and continuously stirred at 50 °C. It was covered with aluminum foil to reduce solvent evaporation. Once the pellets had completely dissolved (after ∼30 min), the resulting viscous solution was poured onto the wafer and spin-coated at 500 rpm for 60 s to create an approximately 11 μm thick film using a Spincoat G3 by Speedline Technologies, USA. The wafer was dipped into ∼80 ml of EtOH (the nonsolvent) at approximately 4 °C for 30 s to undergo phase inversion. Afterward, the film was rinsed in a large beaker filled with 400 ml of EtOH acting as nonsolvent and continuously stirred at room temperature for 48 h to remove the remaining solvent from the film. The film was peeled off from the aluminum-foil-covered wafer with tweezers, air dried in a fume hood for an additional 24 h and then vacuum baked at approximately 1 Torr and 130 °C for 24 h to remove any residual solvent [13]. Finally, aluminum electrodes, wires and a thermocouple were attached to the film using the same procedure described for the commercial and purified films.

2.2. Characterization

Density and porosity. The effective density of a porous film having porosity ϕ can be expressed as

$$\rho_{\mathrm{f}} = \rho_{\mathrm{d}}(1-\phi) + \rho_{\mathrm{air}}\phi \simeq \rho_{\mathrm{d}}(1-\phi) \tag{1}$$

where ρ_{f}, ρ_{d} and ρ_{air} are the densities of the porous film, the dense P(VDF-TrFE) film and air, respectively. Since $\rho_{\mathrm{d}} \gg \rho_{\mathrm{air}}$, the mass of air in the film can be neglected compared with that of the matrix. Rearranging equation (1) gives the porosity as

$$\phi = \frac{\rho_{\mathrm{d}} - \rho_{\mathrm{f}}}{\rho_{\mathrm{d}}}. \tag{2}$$

The density of each film was determined by calculating the volume and measuring the mass. Thickness was measured using a Dektak 6 profilometer from Veeco Metrology, Inc., USA while the length and width of all films were measured with a caliper from ALLTRADE, USA that had a precision of 25.4 μm. Mass measurements were made using a model AG125 scale by Mettler Toledo, Inc., USA with a precision of 0.1 mg. The average surface roughness was also measured as 1 μm.

DSC analysis. Differential scanning calorimetry (DSC) was performed using a Diamond DSC from Perkin Elmer, USA to determine (i) the ferroelectric to paraelectric and paraelectric to ferroelectric phase transition temperatures, (ii) the associated specific phase change enthalpy Δh and (iii) the specific heat $c_p(T)$ of each sample as a function of temperature T. The specific heat is defined as

$$c_p(T) = \frac{\dot{Q}_{\mathrm{DSC}}}{m\dot{T}} \tag{3}$$

where $\dot{Q}_{\mathrm{DSC}}$ is the heat transfer rate provided to the sample and measured by the DSC (in W), m is the sample mass (in kg) and $\dot{T} = \mathrm{d}T/\mathrm{d}t$ is the heating rate expressed in °C s^{-1}. The error bars shown in figure 3 correspond to a 95% confidence interval.

The instrument was calibrated using an Indium standard purchased from Perkin Elmer, USA. The melting temperature at atmospheric pressure and specific phase change enthalpy were measured to be 156.5 °C and 28.19 J g^{-1}, respectively. These values fall within 0.1% and 1.0% of the Indium data sheet, respectively. The procedure to measure the specific heat c_p was also validated using an aluminum sample. It was found that the value of c_p of aluminum was 0.919 J g^{-1} K^{-1} at 27 °C, falling within 1.8% from data reported in the literature [39].

Electrical resistivity. Resistivity measurements for all films were performed with an electrical circuit that consisted of (1) a high voltage power supply model PS325 from Stanford Research Systems Inc., USA, (2) a Keithley 6512 electrometer and (3) a capacitor with capacitance $C_R = 1.0$ μF in series with (4) the pyroelectric element. Note that C_R was a film capacitor with virtually zero leakage relative to the specimen (∼100 times less) and was chosen to be much larger than C_{film} (∼1 nF). The electrometer measured the voltage V_{E} across the capacitor C_R. Resistivity measurements were conducted at a constant temperature of 95 °C such that no pyroelectric power was generated. Thus, the measured current was equal to the leakage current. The leakage current I_{L}, the voltage across the pyroelectric element V_{PE} and the film resistivity ρ_{R} were computed as

$$I_{\mathrm{L}} = C_R\frac{\mathrm{d}V_{\mathrm{E}}}{\mathrm{d}t}, \quad V_{\mathrm{PE}} = V_{\mathrm{SRS}} - V_{\mathrm{E}}, \quad \text{and} \quad \rho_{\mathrm{R}} = \frac{V_{\mathrm{E}}A}{I_{\mathrm{L}}b}. \tag{4}$$

The thermocouple used to measure the film temperature T was calibrated by measuring, at atmospheric pressure, the temperatures of (i) ice water, (ii) boiling water and (iii) air at room temperature and atmospheric pressure. The error bars shown in figure 4 correspond to a 95% confidence interval.

Resistivity measurement began by placing a pyroelectric film with its thermocouple on a hot plate at 95 °C. The film was thermally insulated and connected to the electrical circuit. After the film temperature reached steady state, the electric field was slowly increased at a rate of 2 MV m^{-1} min^{-1} until an electric field of 10 MV m^{-1} was applied to the film. The voltage V_m was recorded for 230 min. The film was allowed to return to room temperature before the electric field was removed.

FTIR analysis. In order to investigate the possible presence of solvent in the film after the synthesis process for the porous and purified films, FTIR spectroscopy measurements were performed using an FT/IR-420 from Jasco, Japan for wavenumbers between 400 and 4000 cm^{-1}. Measurements were taken with a spectral resolution of 4 cm^{-1} and averaged over 16 runs. The absorption coefficient is defined as

$$\kappa = -\frac{1}{b}\ln\left(\frac{I}{I_0}\right) \tag{5}$$

where b is the film thickness and I/I_0 is the film transmittance.

The spectral calibration of the instrument was performed with a polystyrene calibration film purchased from Perkin Elmer, USA. The absorption peaks at wavenumbers 906.4, 1027.9, 1155.2, 1600.6, 1801.2, 1942.0, 2850.3 and 3025.8 cm^{-1} obtained from the instrument agree within 0.1% with the peaks reported in the literature [40].

Hysteresis curves. The ferroelectric hysteresis behavior of each film was studied using a Sawyer-Tower circuit consisting of (1) a WaveTek 10 MHz function generator model 29, (2) a TREK model 610E high voltage amplifier, (3) a Keithley 6512 electrometer and (4) a capacitor with capacitance $C_1 = 9.6\ \mu$F connected in series with (5) the pyroelectric element. Note that C_1 was chosen to be much greater than the capacitance of the films ($C_{\text{film}} \sim 1$ nF). A triangular wave, output by the function generator, was amplified by the high voltage amplifier and cycled across the pyroelectric element. The electrometer measured the voltage V_E across capacitor C_1. Therefore, the electric displacement D (C m^{-2}) of the pyroelectric material was computed as

$$D = \frac{V_E C_1}{A} \tag{6}$$

where A is the cross-sectional area of the film. Hysteresis measurements were conducted at room temperature with the pyroelectric element placed in 3M™ Fluorinert™ FC-70 dielectric fluid to prevent electrical sparks. The electric field was cycled at a frequency of $f = 0.01$ Hz.

Dielectric constant and loss tangent. The relative dielectric constant ε_r and loss tangent $\tan\delta$ of each film were explored as a function of temperature using an Agilent 4284A Precision LCR meter at a frequency of $f = 1$ kHz. Pyroelectric IR detectors typically operate in this frequency range [1]. The relative dielectric constant is given as

$$\varepsilon_r = \frac{C_{PE} b}{\varepsilon_0 A} \tag{7}$$

where C_{PE} is the capacitance measured by the LCR meter. The error bars shown in figure 6 correspond to a 95% confidence interval.

The calibration of the instrument was checked with a 50.8 μm thick Kapton® HN film. The relative dielectric constant and loss tangent were measured at room temperature to be 3.6 and 0.0018, respectively, at $f = 1$ kHz. These values fall within 6.3 and 7.7% of the manufacturer's data sheet, respectively. Measurements on the synthesized films were taken from room temperature up to 100 °C using a hot plate. To ensure uniform temperature, the films were placed in an insulated glass beaker filled with Dow Corning 200® Fluid 50 cst silicone oil. The fluid temperature was monitored continuously. Measurements were averaged over 10 runs at each temperature.

Pyroelectric coefficient. Pyroelectric coefficients were determined as a function of temperature for all films using the method of charge integration [41, 42] with an electric circuit consisting of (1) an electrometer connected in parallel with (2) the pyroelectric element and (3) a capacitor with capacitance $C_1 = 9.6\ \mu$F. The pyroelectric coefficient is defined as [42]

$$p = \left(\frac{\partial D}{\partial T}\right)_{\sigma,E} \tag{8}$$

where σ is stress and E is the electric field. Experimentally, σ was kept constant by not clamping or constraining the deformation of the films. Note that, in general, the pyroelectric coefficient is a vector, but since all samples were poled perpendicular to the plane of the electrodes, only its magnitude is reported. In the method of charge integration, the pyroelectric film was heated over a small temperature range (∼3 °C) around the temperature of interest while the voltage was measured by an electrometer. Therefore, the pyroelectric coefficient was experimentally determined as

$$p \approx \frac{\Delta D}{\Delta T} = \frac{\Delta V_{PE} C_1}{A \Delta T}. \tag{9}$$

The error bars shown in figure 7 correspond to a 95% confidence interval.

All films were poled before measurements were taken. The poling process was adapted from Yamazaki *et al* [24] who showed that poling under DC fields at elevated temperatures can significantly improve the pyroelectric coefficient of P(VDF-TrFE). Poling began by heating the films to 70 °C and then applying a constant DC field of 20 MV m^{-1} for 5 min. Then, the temperature was slowly reduced to room temperature

Table 1. Summary of all measured properties for commercial, purified and porous $\phi = 33\%$ 60/40 P(VDF-TrFE) thin films.

Material	T (°C)	c_p (J g^{-1} K^{-1})	ε_r (1 kHz)	$\tan\delta$ (1 kHz)	p (C m^{-2} K^{-1} $\times 10^{-5}$)	ε_r (0.01 Hz)	ρ (23 °C) (kg m^{-3})	$T_{peak,fp}$ (°C)	$T_{peak,pf}$ (°C)	Δh_{fp} (J g^{-1})	Δh_{pf} (J g^{-1})	ρ_R (95 °C) (Ω m $\times 10^{10}$)
Commercial	25	1.70	17.9	0.041	4.50	28.8	1879	65.7	59.7	8.9	8.4	5.41
	40	1.79	29.7	0.047	7.27							
	50	1.88	37.7	0.045	14.33							
	60	2.16	88.5	0.042	11.76							
	65	3.81	96.8	0.032	6.62							
	70	2.16	89.9	0.026	2.48							
	80	2.05	78.4	0.027	0							
	90	2.05	67.2	0.030	—							
	100	2.08	57.9	0.037	—							
Purified	25	1.44	19.4	0.042	5.09	28.8	1575	65.1	59.8	6.3	6.2	2.06
	40	1.51	27.7	0.051	9.94							
	50	1.58	33.6	0.055	14.77							
	65	2.98	76.2	0.046	4.49							
	70	1.76	83.8	0.037	0							
	80	1.66	71.0	0.028	—							
	90	1.67	61.2	0.006	—							
	100	1.76	52.0	0.010	—							
Porous, $\phi = 33\%$	25	1.47	19.5	0.039	4.30	39.9	1251	66.9	60.3	7.3	6.9	0.75
	40	1.56	29.6	0.047	6.64							
	50	1.65	39.0	0.049	10.63							
	60	1.89	68.9	0.050	3.47							
	65	2.42	77.6	0.039	0							
	70	2.13	76.3	0.011	—							
	80	1.78	66.9	0.052	—							
	90	1.80	60.3	0.017	—							
	100	1.85	53.4	0.022	—							

when the DC field was removed. The poling temperature and time were chosen after Yamazaki *et al* [24], who established that higher temperatures and longer times did not show further improvement in the pyroelectric coefficient.

Measurements began by heating a thermally insulated container filled with silicone oil to the desired temperature and another one at 3 °C higher. Here also the fluid was stirred and a thermocouple was used to continuously monitor its temperature. The P(VDF-TrFE) sample was alternately dipped from one bath to the other while the voltage was recorded. Sufficient time was allowed for the temperature of the sample to equilibrate with that of the fluid before transferring the sample to the other beaker. Measurements were repeated four times for each temperature and averaged.

3. Results and discussion

The thermophysical and electrical properties of the synthesized commercial, purified and porous P(VDF-TrFE) thin films are presented in the following subsections. Properties characterized include (1) density, (2) ferroelectric to paraelectric phase transition temperature, (3) enthalpy of change of phase, (4) electrical resistivity and (5) ferroelectric hysteresis, as well as (6) specific heat, (7) dielectric constant, (8) loss tangent and (9) pyroelectric coefficient as a function of temperature. All properties measured for each type of film at different temperatures are summarized in table 1.

3.1. Density and porosity

The density of the dense commercial P(VDF-TrFE) films was experimentally determined to be $\rho_d = 1879 \pm 39$ kg m^{-3} with a 95% confidence interval. This value is reasonable, considering that a 70/30 P(VDF-TrFE) film was reported to have a density of 1917 kg m^{-3} [27]. The purified films had a density of $\rho_d = 1575 \pm 30$ kg m^{-3} with a 95% confidence interval. The smaller density of the purified films may suggest a porous structure with a porosity of $\phi = 16\% \pm 4\%$. To explore the presence of pores or voids in the purified films, scanning electron microscopy (SEM) images are presented in the following section. The density of the porous films was calculated to be $\rho_f = 1251 \pm 64$ kg m^{-3} with a 95% confidence interval. Thus, the porosity of porous films made from a 15 wt% solution of P(VDF-TrFE) in MEK was $\phi = 33\% \pm 7\%$. Note that, for the given solvent, nonsolvent and copolymer, the porosity of the porous films did not vary by changing the experimental conditions. In general, porosity can be varied by changing the type of solvent and/or nonsolvent used in the phase inversion process. However, the choice of solvent and nonsolvent also affects the pore morphology which can strongly influence the electrical properties of the resulting films. Therefore, a systematic study of the affect of porosity on the thermal and electrical properties of the porous films was not possible.

3.2. SEM micrographs

SEM images of the commercial, purified and porous films were taken using a JSM-6700F field emission SEM from JEOL, Japan. Figure 1(a) depicts the microstructure of the dense commercial film, showing a smooth surface with no voids or cavities. An SEM image of the purified film is shown in figure 1(b). It reveals the presence of small voids

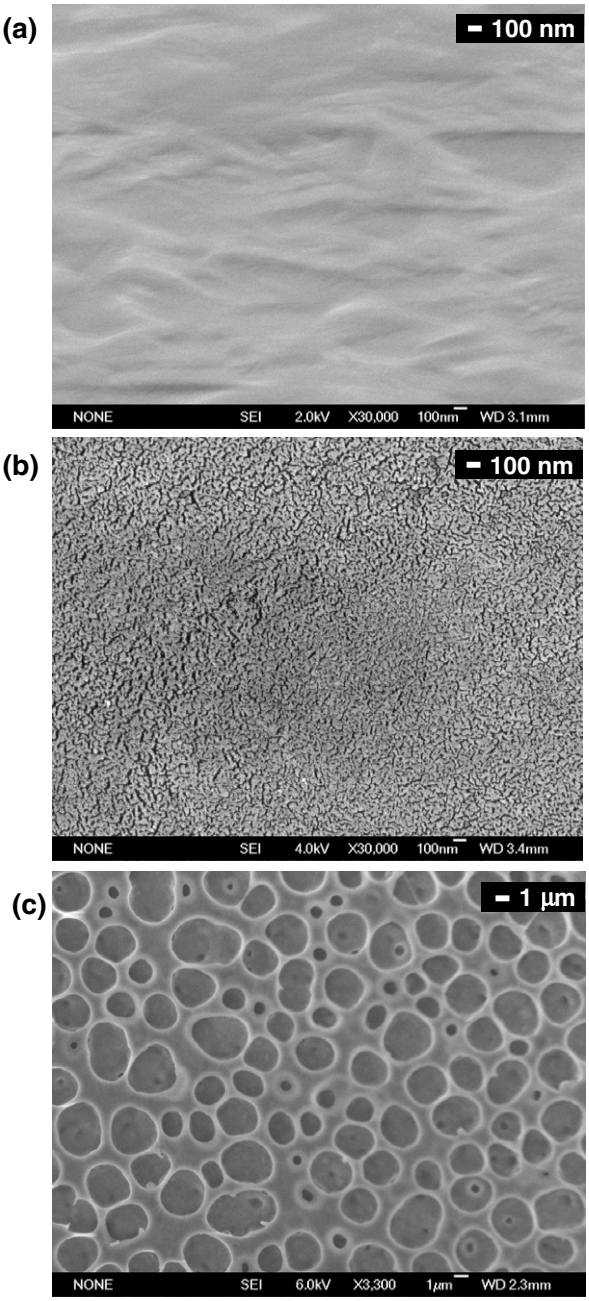

Figure 1. SEM images of (a) commercial, (b) purified and (c) porous ($\phi = 33\%$) 60/40 P(VDF-TrFE) thin films.

approximately 10–20 nm in width. As a result, the purification process creates a porous P(VDF-TrFE) structure. Finally, figure 1(c) illustrates the pore morphology and structure for a porous film with a porosity of 33%. The pores have an average diameter of 2.2 μm with a standard deviation of 0.8 μm. Note that the average pore diameter reported is based on measurements made on the top surface of the film and serves only as an approximation to the actual pore size.

3.3. DSC measurements

Phase transition temperatures. DSC measurements were performed on unpoled samples. Figure 2 plots the heat transfer rate per unit mass $\dot{Q}_{\mathrm{DSC}}/m$ as a function of temperature

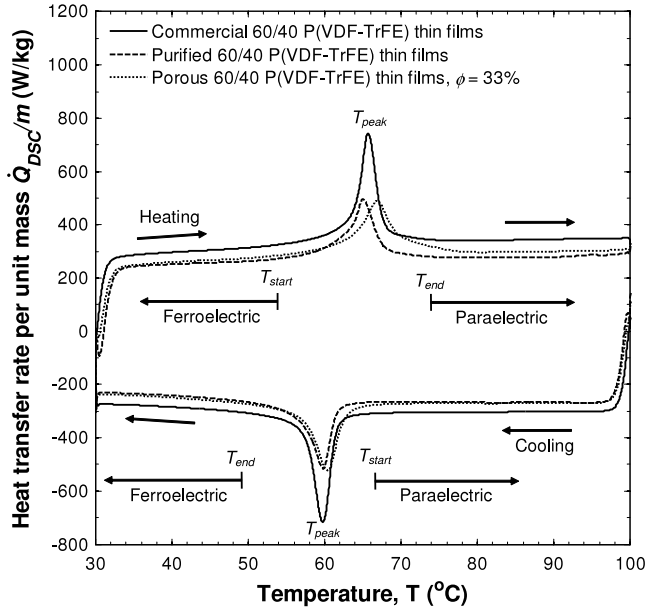

Figure 2. Heat transfer rate per unit mass $\dot{Q}_{\mathrm{DSC}}/m$ versus temperature for commercial, purified and porous ($\phi = 33\%$) 60/40 P(VDF-TrFE) thin films.

T. Each film was heated from 30 to 100 °C at a rate of 10 °C min^{-1}. During heating, the heat transfer rate $\dot{Q}_{\mathrm{DSC}}/m$ exhibited peaks for the commercial, purified and porous films at 65.7, 65.1 and 66.9 °C, respectively. These peaks represent the ferroelectric to paraelectric phase transition of each material. Similarly, each film was then cooled from 100 to 30 °C at a rate of 10 °C min^{-1}. During cooling, the commercial, purified and porous films exhibited peaks at 59.7, 59.8 and 60.3 °C, respectively. The peaks represent the paraelectric to ferroelectric phase transition. In addition, figure 2 reveals that (1) the ferroelectric to paraelectric phase transition upon heating occurred at a higher temperature than the paraelectric to ferroelectric phase transition upon cooling and (2) both transitions occurred over a relatively wide temperature range.

The average starting T_{start} and ending T_{end} temperatures of both phase transitions, along with the peak temperature T_{peak}, are also shown in figure 2. The ferroelectric to paraelectric phase transition temperature was nearly the same for all films with an average value of 65.9 °C. Likewise, the para-to ferroelectric phase transition temperature was about the same for all films with an average value of 59.9 °C. Both phase transition temperature ranges (T_{start}–T_{end}) for all films were about the same with an average value of 22.4 °C. This establishes that neither purification nor the presence of pores in the matrix have a large impact on the phase transition peak temperatures or temperature ranges.

Specific phase change enthalpy. The ferro- to paraelectric phase change enthalpy Δh_{fp} was 8.9, 6.3 and 7.3 J g^{-1} for the commercial, purified and porous films, respectively. The corresponding para- to ferroelectric phase change enthalpy Δh_{pf} was 8.4, 6.2 and 6.9 J g^{-1}, respectively. In other words,

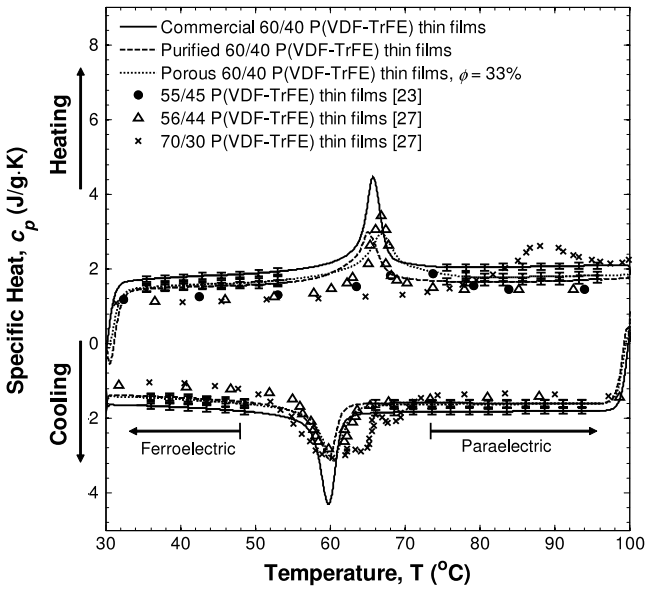

Figure 3. Specific heat versus temperature for commercial, purified and porous ($\phi = 33\%$) 60/40 and 55/44 [23], 56/44 and 70/30 [27] P(VDF-TrFE) thin films.

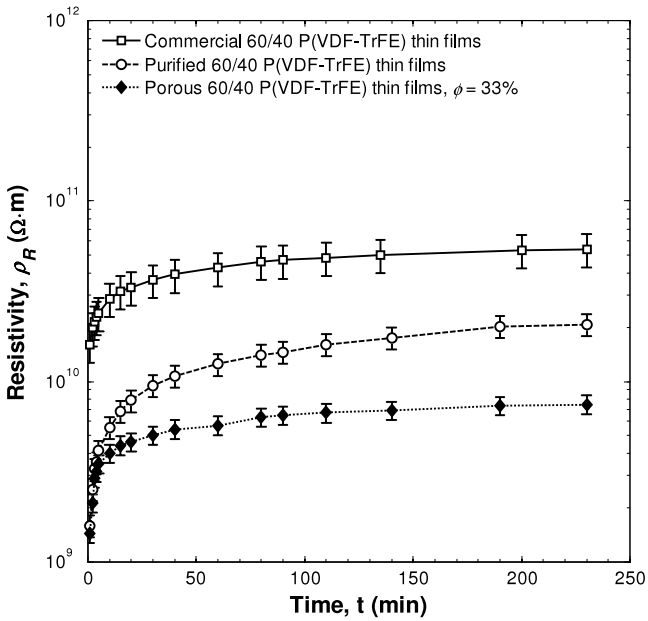

Figure 4. Resistivity versus time at 95 °C and 10 MV m^{-1} for the commercial, purified and porous ($\phi = 33\%$) 60/40 P(VDF-TrFE) thin films.

the purified and porous films had a phase change enthalpy approximately 28 and 18% lower than that of the commercial films, respectively. The phase change enthalpy is related to the size of the ferroelectric phase in the film. A larger value implies the presence of a larger ferroelectric phase. Kouchachvili *et al* [15] reported Δh_{fp} of 4.6 and 7.1 J g^{-1} for commercial and purified 60/40 P(VDF-TrFE) films, respectively. Note that the authors did not perform the vacuum bake out recommended by Olsen *et al* [13].

Specific heat. Figure 3 plots the specific heat $c_p(T)$ as a function of temperature T. It was measured by heating each film from 30 to 100 °C, followed by cooling from 100 to 30 °C. Each film exhibited a peak in c_p at the phase transition temperatures measured by the DSC. The specific heat of the purified and porous films was approximately 14.9 and 12.0% lower than that of the commercial films, respectively. Data for 55/45 [23], 56/44 and 70/30 [27] P(VDF-TrFE) films are also presented for comparison. Note that the ferro- to paraelectric phase transition shifts to higher temperature for the 70/30 P(VDF-TrFE) film. The effective specific heat of the porous films is in good agreement with the following expression:

$$c_{p,\mathrm{porous}}(T) = (1-\phi)c_{p,\mathrm{d}}(T) + c_{p,\mathrm{air}}\phi \qquad (10)$$

where $c_{p,\mathrm{d}}$ and $c_{p,\mathrm{air}}$ are the specific heat of the dense phase and air, respectively. If one considered $c_{p,\mathrm{d}}(T)$ measured for the commercial films for all temperatures and $c_{p,\mathrm{air}} = 1.008$ J g^{-1} K^{-1} at 77 °C [39], equation (10) predicts the experimental data for the porous films within 6.3% for temperatures below and above the ferro- to paraelectric and para- to ferroelectric phase transitions. Equation (10) was also applied to the purified films that had a porosity of 16% and the predicted c_p was within 18.3% of the measured data.

3.4. Electrical resistivity

Figure 4 plots the resistivity of each film as a function of time measured at 95 °C and 10 MV m^{-1}. It shows that the commercial films have the highest resistivity followed by the purified and porous ($\phi = 33\%$) films. In the first 15 min, the resistivity of all films increased rapidly by approximately a factor of 2.0, 4.3 and 3.1 for the commercial, purified and porous films, respectively. After 100 min, the resistivity of these films increased respectively at an average rate of approximately 47.8, 40.9 and 6.7 MΩ m min^{-1}. Finally after 230 min, their resistivity reached 5.41, 2.06 and 0.75 × 10^{10} Ω m, respectively. A possible mechanism for the observed increase in resistivity over time is the accumulation of ionic charge carriers under the electrodes which would cancel the electric field within the film and reduce the leakage current.

Kouchachvili *et al* [15] reported a resistivity of 0.57 and 1.02 × 10^{12} Ω m after 90 min for commercial and purified 60/40 P(VDF-TrFE) films, respectively. The measured resistivity in this study at 90 min for the commercial and purified films was 4.70 and 1.45 × 10^{10} Ω m, respectively. Consequently, the results for the purified films shown in figure 4 contradict results reported by Kouchachvili *et al* [15]. Indeed, the authors claimed a 35% increase in resistivity for the purified films compared with the commercial films. Note that they did not use an electrometer which can affect the accuracy of their measurements. It remains unclear how 'approximately 0.4% of unidentifiable impurities' were removed [15] if one does not have specific knowledge about these impurities. One possibility for the reduction in resistivity measured for the purified films could be the presence of MEK solvent in the films. To explore this, FTIR spectroscopy measurements were performed to determine if solvent remained in the purified and porous films after synthesis. No observable trace of

residual solvent was seen. Another explanation for the reduced resistivity of both the purified and porous films is due to the presence of pores in the films, as shown in figure 1. The interface between the matrix and pores creates electric field gradients in the surrounding area near the pores. As a result, the field is concentrated in regions between pores and the film can locally experience fields larger than the applied field. This argument supports the results in figure 4. The purified films with a porosity of 16% and pore size of about 15 nm had a larger resistivity than the porous films with porosity of 33% and pore size of 2 μm.

3.5. Hysteresis curves

Figure 5(a) plots the electric displacement versus applied electric field of the purified films. At $f = 0.01$ Hz, the top and bottom of the loop are rounded, indicating the presence of resistive losses caused by current leakage through the films during the measurement. Indeed, at a higher frequency of 0.1 Hz, the top and bottom of the loop are no longer rounded. To account for leakage at lower frequencies, the electric displacement due to resistive losses D_L can be calculated using Ohm's law as

$$D_L(t) = \int_0^t \frac{E(\tau)b}{R}\,\mathrm{d}\tau \tag{11}$$

where τ is an integration variable. Applying equation (11) to the experimental data at $f = 0.01$ Hz produces the '0.01 Hz corrected' loop shown in figure 5(a), which matches very well with the measurement at $f = 0.1$ Hz. As a result, the resistive losses in the copolymer are linear and obey Ohm's law.

Figure 5(b) plots the ferroelectric hysteresis behavior at $f = 0.01$ Hz for the commercial, purified and porous P(VDF-TrFE) thin films where equation (11) was used to correct for resistive losses. Data for 65/35 and 73/27 P(VDF-TrFE) films are also included from Davis *et al* [26] at $f = 0.0167$ Hz. The room temperature hysteresis curves for all films are similar to each other. The figure reveals that the commercial, purified and porous films have about the same coercive field of $E_c = 30.5$ MV m^{-1}, indicating that neither purification nor the presence of pores in the matrix have a large effect on E_c. Furthermore, the purified and porous films exhibit larger polarization than that of the commercial films as seen by the greater maximum electric displacement D in figure 5(b). In addition, the relative dielectric constant ε_r at $f = 0.01$ Hz and room temperature was determined by calculating the slope of each curve in figure 5(b) as

$$\varepsilon_r = \frac{1}{\varepsilon_0}\left(\frac{\partial D}{\partial E}\right)_{\sigma,T} \tag{12}$$

where ε_0 is the vacuum permittivity equal to 8.854×10^{-12} F m^{-1}. The relative dielectric constants of the commercial and purified films, computed using equation (12) in the saturation region, were about the same with an average value of $\varepsilon_r = 28.8$ while that for the porous films was $\varepsilon_r = 39.9$.

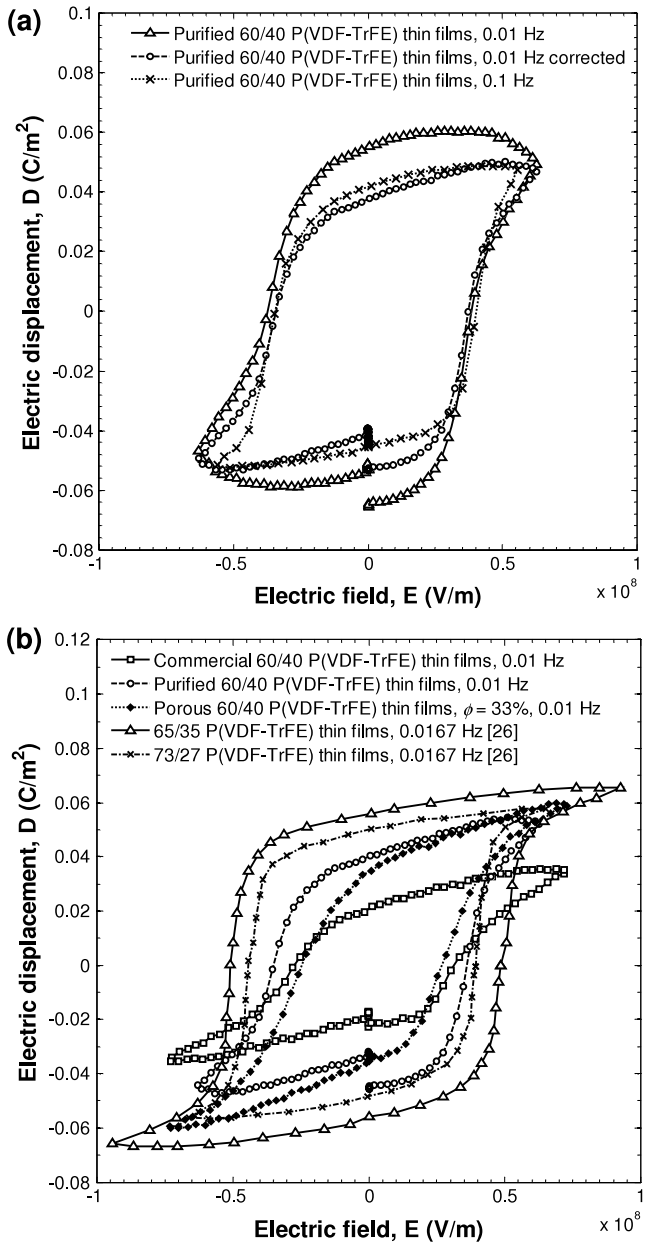

Figure 5. Electric displacement versus applied electric field for (a) purified films as a function of frequency and (b) corrected for leakage at 0.01 Hz for commercial, purified and porous ($\phi = 33\%$) 60/40 P(VDF-TrFE) thin films. Data for 65/35 and 73/27 P(VDF-TrFE) at 0.0167 Hz [26] is also included.

3.6. Dielectric constant and loss tangent

Figure 6 plots the relative dielectric constant ε_r and loss tangent $\tan\delta$ of each film as a function of temperature at $f = 1$ kHz from room temperature to 100 °C. Note that error bars for some data points are smaller than the size of data markers and are not visible in the figure. At room temperature, the commercial films had $\varepsilon_r = 17.9$, which is comparable to the value of 18 reported by Lang *et al* [1] for dense 50/50 P(VDF-TrFE) while for the purified and porous films, $\varepsilon_r = 19.4$ and 19.5, respectively. As a result, ε_r for the commercial, purified and porous films was about 38, 33 and 51% less, respectively, than that determined from the slope of each curve

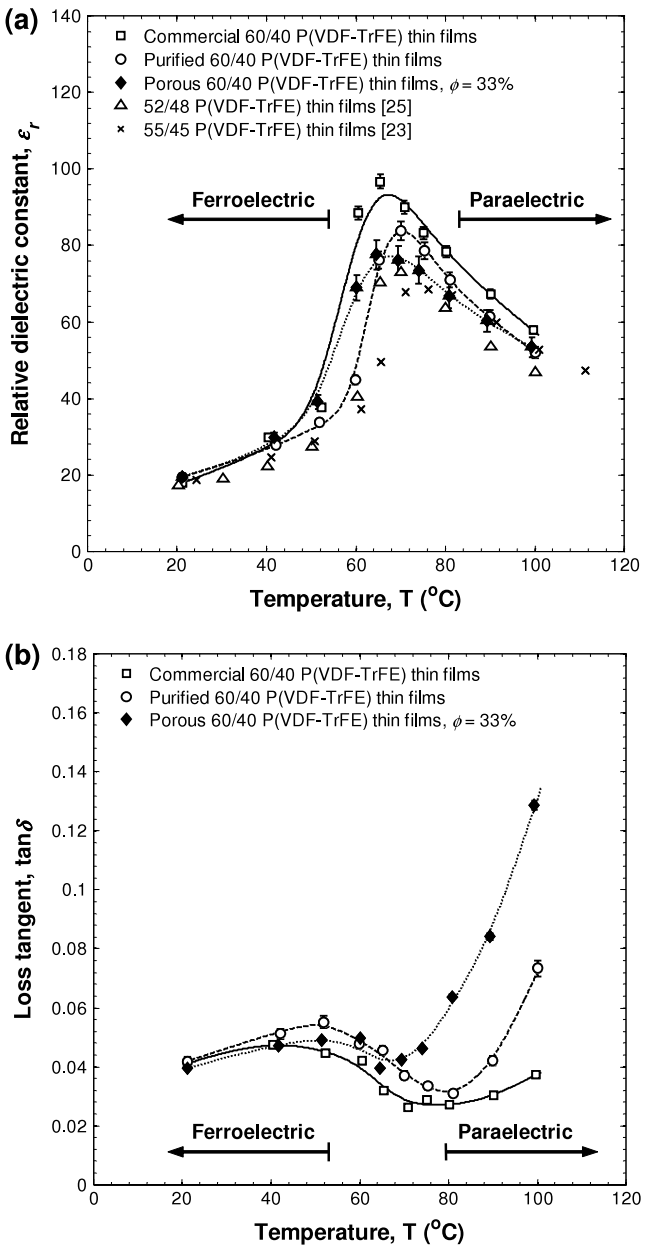

Figure 6. (a) Relative dielectric constant and (b) loss tangent versus temperature at 1 kHz for commercial, purified and porous ($\phi = 33\%$) 60/40 P(VDF-TrFE) thin films. Results for 52/48 [25] and 55/45 [23] P(VDF-TrFE) are also included.

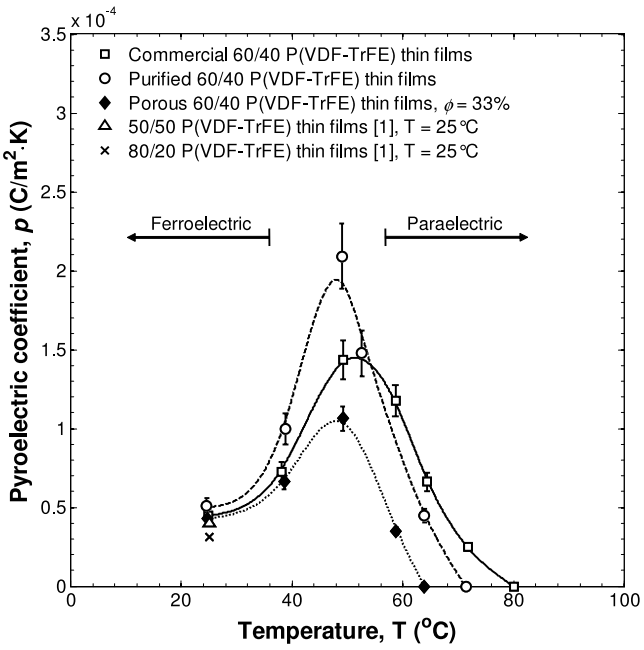

Figure 7. Pyroelectric coefficient versus temperature for commercial, purified and porous ($\phi = 33\%$) 60/40 P(VDF-TrFE) thin films. Results for 50/50 and 80/20 P(VDF-TrFE) are also included from [1].

in figure 5(b) at 0.01 Hz. Therefore, ε_r decreases as frequency increases for all films. The relative dielectric constant of the commercial, purified and porous films increased as a function of temperature and exhibited peaks of 96.8, 83.8 and 77.6 at temperature 65.5, 70.1 and 64.6 °C, respectively. These temperatures agree well with those associated with the peaks of the ferroelectric to paraelectric phase transition seen in figure 2. As the temperature was further increased, ε_r began to decrease for all films. The trend and magnitude in ε_r agrees well with data for 52/48 [25] and 55/45 [23] P(VDF-TrFE) films.

The loss tangent of the commercial films at room temperature was 0.041, which is reasonable considering that dense 50/50 P(VDF-TrFE) was reported to have $\tan\delta = 0.035$ [1] at $f = 1$ kHz. The loss tangent of the commercial, purified and porous films increased as a function of temperature up to an inflection point around 65.5, 70.1 and 64.6 °C, respectively. These temperatures are identical to those when ε_r reaches a maximum. Beyond this inflection point, $\tan\delta$ increases with temperature to reach 0.037, 0.073 and 0.129 for the commercial, purified and porous films, respectively.

3.7. Pyroelectric coefficient

Figure 7 plots the pyroelectric coefficient p as a function of temperature for the three types of films. At room temperature, p for the commercial, purified and porous films was 4.5, 5.1 and 4.3 $\times$ 10^{-5} C m^{-2} K^{-1}, respectively. For the commercial films, the measured value of p is comparable to 4.0 $\times$ 10^{-5} C m^{-2} K^{-1} for dense 50/50 P(VDF-TrFE) reported by Lang *et al* [1]. Figure 7 shows that the pyroelectric coefficient of the commercial, purified and porous films increases as a function of temperature and all films exhibited peaks of 1.4, 2.1 and 1.2 $\times$ 10^{-4} C m^{-2} K^{-1} around 50 °C, respectively. The peak temperature agrees well with the start of the ferroelectric to paraelectric phase transition shown in figure 2. For higher temperatures, the pyroelectric coefficient rapidly decreased. Indeed, the films lose their polarization as they are heated through the phase transition. Furthermore, figure 7 shows that the purified films had the largest pyroelectric coefficients while the porous films had the smallest ones.

3.8. Figures of merit

Different figures of merit (FOM) exist to assess the performance of pyroelectric materials depending on the

application considered. For infrared detectors, the (1) voltage F_V, (2) current F_I and (3) noise F_D figures of merit are defined as [1]

$$F_V = \frac{p}{\rho c_p \varepsilon_0 \varepsilon_r}, \qquad F_I = \frac{p}{\rho c_p}, \qquad \text{and} \qquad F_D = \frac{p}{\rho c_p \sqrt{\varepsilon_0 \varepsilon_r \tan\delta}} \tag{13}$$

F_V gives a measure of the ratio of the output voltage response of the detector to the input power defined as the radiation incident on the surface of the detector. Likewise, F_I represents the pyroelectric current generated per watt of input power. The third figure of merit, F_D, quantifies electrical noise caused by thermal energy (Johnson noise), usually the primary source of noise in pyroelectric infrared detectors [1].

For energy harvesting, two figures of merit have been proposed, namely F_E [19] and k^2 defined as [20]

$$F_E = \frac{p^2}{\varepsilon_0 \varepsilon_r}, \qquad \text{and} \qquad k^2 = \frac{p^2 T_{hot}}{\rho c_p \varepsilon_0 \varepsilon_r} \tag{14}$$

where T_{hot} is the temperature of the hot source. F_E represents how much electrical power a pyroelectric material can harvest from the hot source while k^2 is a dimensionless electrothermal coupling factor that represents how effectively a pyroelectric material converts thermal energy into electrical energy.

Infrared detection. Figure 8(a) plots the voltage figure of merit F_V as a function of temperature for each film. Note that F_V and F_D were computed using the dielectric constant measured in section 3.6 since pyroelectric infrared detectors typically operate near 1 kHz [1]. In addition, for the computation of all figures of merit, the density was assumed to be constant and equal to the value measured at room temperature. At 25 °C, F_V for the commercial, purified and porous films was 0.09, 0.13 and 0.14 m^2 C^{-1}, respectively. This corresponds to an increase by 47.0 and 52.8% for the purified and porous films, respectively, compared with that of the commercial films. The improved performance of the purified films was due to its higher pyroelectric coefficient and smaller value of ρc_p. The reduction in ρc_p for the porous films was responsible for the increase in F_V. For comparison, F_V for 50/50 and 80/20 P(VDF-TrFE) films was 0.11 and 0.22 m^2 C^{-1}, respectively, at room temperature [1]. Note that the authors used ρc_p of PVDF (2.3×10^6 J m^{-3} K^{-1}) for their computations: however, ρc_p of P(VDF-TrFE) can be much larger, thus reducing F_V. For example, $\rho c_p = 3.2 \times 10^6$ J m^{-3} K^{-1} at room temperature for the commercial 60/40 P(VDF-TrFE) films. As the temperature increased to 40 °C, F_V decreased for the commercial and porous films since $c_p \varepsilon_r$ increased at a faster rate than p. With further increase in temperature, F_V increased for the commercial, purified and porous films which exhibited peaks of 0.12, 0.20 and 0.16 m^2 C^{-1} around 50 °C, respectively.

Figure 8(b) plots the current figure of merit F_I as a function of temperature for each film. At room temperature, F_I for the commercial, purified and porous films was 1.41, 2.25 and 2.34 $\times$ 10^{-11} m V^{-1}, respectively. Thus, F_I for the purified and porous films was 59.6 and 66.3% greater, respectively, than that of the commercial films. For 50/50 and 80/20 P(VDF-TrFE) films, F_I was reported to be 1.7 and 1.3×10^{-11} m V^{-1}, respectively, at room temperature [1]. As temperature increased, F_I increased for all films and peaks of

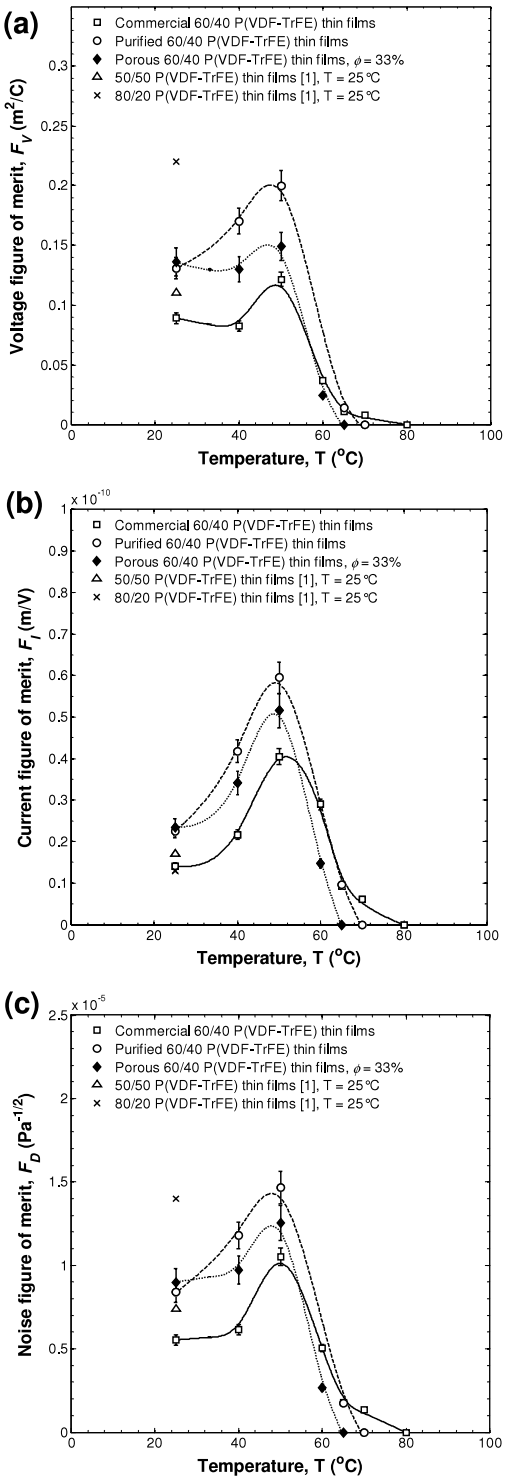

Figure 8. (a) Voltage, (b) current and (c) noise figure of merit for infrared detection as a function of temperature for commercial, purified and porous ($\phi = 33\%$) 60/40 P(VDF-TrFE) thin films. Results for 50/50 and 80/20 P(VDF-TrFE) are also included from [1].

4.05, 5.95 and 5.56 $\times$ 10^{-11} m V^{-1} existed around 50 °C for the commercial, purified and porous films, respectively.

Figure 8(c) plots the noise figure of merit F_D as a function of temperature for each film. At room temperature, F_D for the commercial, purified and porous films was 5.53, 8.38 and 8.99×10^{-6} $Pa^{-1/2}$, respectively. Therefore, F_D for the purified and porous films was 51.6 and 62.6% greater, respectively, than that of the commercial films, signifying a reduction in noise when used for infrared detection. The results are comparable to 7.4 and 14×10^{-6} $Pa^{-1/2}$ for 50/50 and 80/20 P(VDF-TrFE) films, respectively, at room temperature [1]. F_D increased as a function of temperature and peaks of 1.05, 1.47 and 1.35 $\times$ 10^{-5} $Pa^{-1/2}$ were apparent around 50 °C for the commercial, purified and porous films, respectively.

Energy harvesting The figure of merit F_E and the factor k^2 were computed near room temperature where the material behavior is linear. The dielectric constant measured at low frequency reported in section 3.5 was used. For the commercial, purified and porous films, F_E was 7.93, 10.17 and 5.24 J m^{-3} K^{-2}, respectively. For the purified films, F_E was greater than that of the commercial films due to its larger pyroelectric coefficient. However, F_E for the porous films was smaller than for the commercial films due to its smaller pyroelectric coefficient.

The factor k^2 near room temperature was 0.93, 1.68 and 1.06 $\times$ 10^{-3} for the commercial, purified and porous films, respectively. Note that T_{hot} was chosen as 100 °C since energy conversion with P(VDF-TrFE) focuses on low temperature waste heat and leakage current can become significant at higher temperatures. For the purified and porous films, k^2 was 80.7 and 14.8% greater than that of the commercial films, respectively. The improvement was due to the reduction in heat capacity ρc_p and to the larger pyroelectric coefficient of the purified films. The results suggest that energy harvesting achieved with purified and porous films can be more efficient than with the commercial films.

4. Conclusion

This work aimed at characterizing the electrical and thermophysical properties of 60/40 P(VDF-TrFE) to help achieve higher performance for pyroelectric IR detectors and energy harvesting devices. Commercial, purified and porous P(VDF-TrFE) films were prepared and characterized. It was established that:

(i) the peak temperature during the ferro- to paraelectric and para- to ferroelectric phase transitions was around 65.9 and 59.9 °C, respectively, for all films. This established that neither purification nor the presence of pores in the matrix had a large effect on the phase transition temperatures,

(ii) the ferro- to paraelectric and para- to ferroelectric phase transitions took place over a temperature range nearly the same for all films and equal to 22.6 °C between 53.3 and 75.9 °C and 22.3 °C between 43.4 and 65.7 °C, respectively,

(iii) the phase change enthalpy during the ferro- to paraelectric and para- to ferroelectric phase transitions for purified and porous films was about 28 and 18% lower than that of the commercial films, respectively,

(iv) the specific heat of the porous and purified films was comparable to one another and smaller than that of the commercial films,

(v) electrical resistivity measurements determined that the commercial films had the highest resistivity (5.41 $\times$ 10^{10} Ω m), followed by the purified (2.06×10^{10} Ω m) and then porous films (0.75×10^{10} Ω m). The lower resistivity of the purified and porous films can be attributed to the presence of pores in both films which creates nonuniform electric fields in the films,

(vi) the ferroelectric hysteresis curves established that all films had about the same coercive field of $E_c = 30.5$ MV m^{-1}. Moreover, the purified and porous films exhibited larger polarization than the commercial films,

(vii) at room temperature, the pyroelectric coefficient for the commercial, purified and porous films was 4.5, 5.1 and 4.3 $\times$ 10^{-5} C m^{-2} K^{-1}, respectively. The pyroelectric coefficient for all films reached a maximum at 50 °C corresponding to the start of the ferro- to paraelectric phase transition,

(viii) for all temperatures below the start of the phase transition, the purified films had the largest pyroelectric coefficients that were, on average, about 32% greater than that of the commercial films while the porous films had the smallest values,

(ix) the figures of merit for infrared detection F_V, F_I and F_D were improved by 47.0, 59.6 and 51.6%, respectively, for the purified films. The porous films with $\phi = 33\%$ showed an improvement of 52.8, 66.3 and 62.6%, respectively,

(x) the electrothermal coupling factor k^2 for the purified and porous films was 80.7 and 14.8% greater, respectively, than that of the commercial films. This suggests that purified and porous films can harvest waste heat more efficiently.

The results indicate that porosity reduced the heat capacity ρc_p which improved the thermal response of the films; however, it also reduced the electrical resistivity and pyroelectric coefficient. Thus, porosity can be tuned to achieve the optimum response for a given application. Future work should focus on the molecular structure and constitutive ferroelectric modeling of each type of film to better understand the material behavior. Furthermore, the energy harvesting FOMs were developed assuming linear material behavior subjected to small temperature and voltage changes. To maximize the energy harvested, large changes in displacement are necessary, which result in nonlinear behavior. Thus, there is a need to develop new FOMs to account for nonlinear effects and phase transitions.

Acknowledgments

This work was funded in part by the Office of Naval Research under Award N000140710671 (Program Manager: Dr Mark

Spector), by the NSF IGERT Materials Creation Training Program under grant no. DGE-0114443, and by the Army Research Office through grant W911NF0810230. The authors would like to thank Dr R B Olsen, Dr I Martini and Mr D Vanderpool for useful discussions and exchange of information.

Appendix. Nomenclature

A	surface area of pyroelectric element, m^2
b	thickness of pyroelectric element, m
c_p	specific heat, J g^{-1} K^{-1}
C	capacitance, F
D	electric displacement, C m^{-2}
D_L	electric displacement associated with resistive losses, C m^{-2}
E	electric field, V m^{-1}
E_c	coercive field, V m^{-1}
f	frequency, Hz
F_D	noise figure of merit, $Pa^{-1/2}$
F_E	energy harvesting figure of merit, J m^{-3} K^{-2}
F_I	current figure of merit, m V^{-1}
F_V	voltage figure of merit, m^2 C^{-1}
h	enthalpy of change of phase, J g^{-1}
I/I_0	film transmittance
I_L	leakage current, A
k^2	electrothermal coupling factor
L	length of pyroelectric element, m
m	mass, kg
p	pyroelectric coefficient, C m^{-2} K^{-1}
$\dot{Q}_{DSC}$	heat transfer rate measured by DSC, W
R_D	resistance used to measure resistivity, Ω
t	time, s
$\tan\delta$	loss tangent
T	temperature, °C or K
$\dot{T}$	heating rate, °C s^{-1}
V_E	voltage measured by electrometer, V
V_{SRS}	voltage output from the high voltage power supply, V
W	width of pyroelectric element, m

Greek symbols

ε_0	vacuum permittivity, F m^{-1}
ε_r	relative dielectric constant
ϕ	porosity
κ	absorption coefficient, cm^{-1}
ρ	density, kg m^{-3}
ρ_R	electrical resistivity, Ω m
σ	mechanical stress, Pa
τ	integration variable, s

Subscripts

air	refers to air
d	refers to dense film
end	refers to end of phase transition
f	refers to porous film
fp	refers to ferroelectric to paraelectric phase transition
hot	refers to hot source
pf	refers to paraelectric to ferroelectric phase transition
peak	refers to peak of phase transition
PE	refers to pyroelectric element
start	refers to start of phase transition

References

[1] Lang S B and Das-Gupta D K 2001 *Handbook of Advanced Electronic and Photonic Materials and Devices* vol 4 (San Diego, CA: Academic)
[2] Day G W, Hamilton C A, Peterson R L, Phelan R J Jr and Mullen L O 1974 Effects of poling conditions on responsitivity and uniformity of polarization of PVF_2 pyroelectric detectors *Appl. Phys. Lett.* **24** 456–8
[3] Neumann N, Köhler R and Hofmann G 1995 Infrared sensor based on the monolithic structure Si-P(VDF/TrFE) *Ferroelectrics* **171** 225–38
[4] Simonne J J, Bauer F and Audaire L 1995 Pyroelectric properties of a VDF/TrFE-on-silicon sensor *Ferroelectrics* **171** 239–52
[5] Köhler R, Neumann N and Hofmann G 1994 Pyroelectric single-element and linear-array sensors based on P(VDF/TrFE) thin films *Sensors Actuators* A **45** 209–18
[6] Neumann N, Köhler R, Gottfried-Gottfried R and Heß N 1995 Pyroelectric sensors and arrays based on P(VDF/TrFE) copolymer films *Integr. Ferroelectr.* **11** 1–14
[7] Smith B and Amon C 2007 Simultaneous electrothermal test method for pyroelectric microsensors *J. Electron.Packaging* **129** 504–11
[8] Olsen R B, Bruno D A and Briscoe J M 1984 Cascaded pyroelectric energy converter *Ferroelectrics* **59** 205–19
[9] Olsen R B, Bruno D A and Briscoe J M 1985 Pyroelectric conversion cycles *J. Appl. Phys.* **58** 4709–16
[10] Olsen R B, Bruno D A, Briscoe J M and Butler W F 1981 A pyroelectric energy converter which employs regeneration *Ferroelectrics* **38** 975–8
[11] Olsen R B 1982 Ferroelectric conversion of heat to electrical energy—a demonstration *J. Energy* **6** 91–5
[12] Olsen R B and Brown D D 1982 High-efficiency direct conversion of heat to electrical energy related pyroelectric measurements *Ferroelectrics* **40** 17–27
[13] Olsen R B, Bruno D A and Briscoe J M 1985 Pyroelectric conversion cycle of vinylidene fluoride-trifluoroethylene copolymer *J. Appl. Phys.* **57** 5036–42
[14] Ikura M 2002 Conversion of low-grade heat to electricity using pyroelectric copolymer *Ferroelectrics* **267** 403–8
[15] Kouchachvili L and Ikura M 2008 Improving the efficiency of pyroelectric conversion *Int. J. Energy Res.* **32** 328–35
[16] Clingman W H and Moore R G 1961 Application of ferroelectricity to energy conversion processes *J. Appl. Phys.* **32** 675–81
[17] Hoh S R 1963 Conversion of thermal to electrical energy with ferroelectric materials *Proc. IEEE* **51** 838–45
[18] Fatuzzo E, Kiess H and Nitsche R 1966 Theoretical efficiency of pyroelectric power converters *J. Appl. Phys.* **37** 510–6
[19] Sebald G, Seveyrat L, Guyomar D, Lebrun L, Guiffard B and Pruvost S 2006 Electrocaloric and pyroelectric properties of $0.75Pb(Mg_{1/3}Nb_{2/3})O_3$–$0.25PbTiO_3$ single crystals *J. Appl. Phys.* **100** 124112
[20] Sebald G, Pruvost S and Guyomar D 2008 Energy harvesting based on Ericsson pyroelectric cycles in a relaxor ferroelectric ceramic *Smart Mater. Struct.* **17** 1–6
[21] Sebald G, Lefeuvre E and Guyomar D 2008 Pyroelectric energy conversion: optimization principles *IEEE Trans. Ultrason. Ferroelectr. Freq. Control* **55** 538–51
[22] Guyomar D, Pruvost S and Sebald G 2008 Energy harvesting based on FE–FE transition in ferroelectric single crystals *IEEE Trans. Ultrason. Ferroelectr. Freq. Control* **55** 279–85

[23] Furukawa T, Johnson G E and Bair H E 1981 Ferroelectric phase transition in a copolymer of vinylidene fluoride and trifluoroethylene *Ferroelectrics* **32** 61–7
[24] Yamazaki H, Ohwaki J, Yamada T and Kitayama T 1981 Temperature dependence of the pyroelectric response of vinylidene fluoride trifluoroethylene copolymer and the effect of its poling conditions *Appl. Phys. Lett.* **39** 772–3
[25] Furukawa T, Lovinger A J, Davis G T and Broadhurst M G 1983 Dielectric hysteresis and nonlinearity in a 52/48 mol% copolymer of vinylidene fluoride and trifluoroethylene *Macromolecules* **16** 1885–90
[26] Davis G T, Broadhurst M G, Lovinger A J and Furukawa T 1984 Hysteresis in copolymers of vinylidene fluoride and trifluoroethylene *Ferroelectrics* **57** 73–84
[27] Wong Y W, Hui N M, Ong E L, Chan H L W and Choy C L 2003 Specific heat and thermal diffusivity of vinylidene fluoride/trifluoroethylene copolymers *J. Appl. Polym. Sci.* **89** 3160–6
[28] Whatmore R W 1986 Pyroelectric devices and materials *Rep. Prog. Phys.* **49** 1335–86
[29] Kouchachvili L and Ikura M 2006 Pyroelectric conversion-effects of P(VDF-TrFE) preconditioning on power conversion *J. Electrostat.* **65** 182–8
[30] Kouchachvili L and Ikura M 2006 High performance pyroelectric converter *Proc. 6th IASTED Int. Conf. European Power and Energy Systems (Rhodes, June 2006)* p 521-041
[31] Kouchachvili L and Ikura M 2006 High performance P(VDF-TrFE) copolymer for pyroelectric conversion *US Patent* 7,323,506
[32] Vanderpool D, Yoon J H and Pilon L 2008 Simulations of a prototypical device using pyroelectric materials for harvesting waste heat *Int. J. Heat Mass Transfer* **51** 5052–62
[33] Mulder M 1996 *Basic Principles of Membrane Technology* 2nd edn (Boston, MA: Kluwer–Academic)
[34] Kesting R E 1985 *Synthetic Polymeric Membranes* (New York: McGraw-Hill)
[35] Frommer M A, Lancet D, Lonsdale H K and Podall H E 1972 *Reverse Osmosis Membrane Research* (New York: Plenum)
[36] Koenhen D M, Mulder M H V and Smolders C A 1977 Phase separation phenomena during the formation of asymmetric membranes *J. Appl. Polym. Sci.* **21** 199–215
[37] Guillotin M, Lemoyne C, Noel C and Monnerie L 1977 Physicochemical processes occurring during the formation of cellulose diacetate membranes. research of criteria for optimizing membrane performance. IV. Cellulose diacetate-acetone-organic additive casting solutions *Desalination* **21** 165–81
[38] Bottino A, Camera-Roda G, Capannelli G and Munari S 1991 The formation of microporous polyvinylidene difluoride membranes by phase separation *J. Membr. Sci.* **57** 1–20
[39] Moran M J and Shapiro H N 2004 *Fundamentals of Engineering Thermodynamics* 5th edn (New York: Wiley)
[40] Dolphin D and Wick A 1977 *Tabulation of Infrared Spectral Data* (Hoboken, NJ: Wiley)
[41] Lang S B and Steckel F 1965 Method for the measurement of the pyroelectric coefficient, dc dielectric constant, and volume resistivity of a polar material *Rev. Sci. Instrum.* **36** 929–32
[42] Lang S B 1974 *Sourcebook of Pyroelectricity* (New York: Gordon and Breach)